# COMPUTATION OF ADDED MASS COEFFICIENTS OF DARPA SUBOFF USING TWO DIFFERENT SOLVERS OF OPENFOAM

**Oguzhan KIRIKBAS,** Istanbul Technical University, kirikbas17@itu.edu.tr

## ABSTRACT

Added mass is caused by momentum transfer from accelerating vehicle to surrounding fluid domain and is a function of vehicle geometry and density of fluid. It is especially important for underwater vehicles because technical specifications often require a certain acceleration time and stopping distance. In this study surge added mass of DARPA Suboff is calculated utilizing two different solvers of OpenFOAM. Time dependent velocity profiles are applied to simulate the accelerated motion of the vehicle in transient solver pisoFoam. Results of pisoFoam analysis are validated with the results of potentialFoam. Additionally, sway and heave added masses are computed via this method based on change in kinetic energy of fluid domain due to the motion of body. Results are compared with previous studies based on Boundary Element Method and CFD and demonstrate that potentialFoam is also capable of predicting added mass of an underwater vehicle within a reasonable accuracy.

## KEYWORDS

Keywords: Added mass, DARPA Suboff., OpenFOAM, potentialFOAM

## Nomenclature

| | | | |
|---|---|---|---|
| a | Linear Acceleration | PMM | Planar Motion Mechanism |
| AFF | Anechoic Flow Facility | P | Pressure |
| ASE | Analytical-Semi Empirical | RANS | Reynolds-Averaged Navier Stokes |
| BEM | Boundary Element Method | t | Time |
| $C_f$ | Skin Friction Coefficient | U | Linear Velocity |
| CFD | Computational Fluid Dynamics | $U_\infty$, $U_0$ | Freestream Velocity. |
| CMM | Conning Motion Mechanism | URANS | Unsetady Reynolds Averaged Navier-Stokes |
| $C_p$ | Pressure Coefficient | UV | Underwater Vehicle |
| DARPA | Defence Advanced Research Project Agency | x/L | Nondimensional Position |
| D | Maximum Diameter of the UV | $\beta$ | Turbulence Model Coefficient |
| $D_{sphere}$ | Diameter of the Overset Region | $C_\mu$ | Turbulence Model Coefficient |
| $E_K$ | Kinetic Energy | $\varepsilon$ | Turbulence Dissipation Rate |
| F | Force | $\lambda$ | Scale Factor |
| $f_i$ | External Force | $\nu$ | Effective Viscosity |
| H | Height of UV | $\rho$ | Density |
| I | Turbulence Intensity | $\Phi$ | Velocity Potential |
| k | Turbulence Kinetic Energy | $\Omega$ | Angular Velocity |
| L | Characteristic Length of UV | $\nabla$ | Volume |
| M | Moment | $\varepsilon_{ijk}$ | Levi-Cavita Symbol |
| m | Added Mass | $\overline{U_i' U_j'}$ | Reynolds Stress Term |

## 1. INTRODUCTION

Phenomena of added mass and added moment of inertia emerge during the accelerated motion of a body inside a fluid domain as a result of momentum transferred to the surrounding medium. This virtual mass/inertia is a function of body geometry as well as the density of the medium in which the body is accelerated.

These phenomena are critical because they appear in the motion equations of an UV and are directly related to its acceleration and deceleration performance. Thus, they are among the major considerations in designing the propulsion system. In tensor notation, these motion equations are given by (Techet, 2003) as Equations (1) and (2). Here, F and M represents forces and moments, respectively. U and Ω are linear and angular velocities. m represents the added mass, and $\varepsilon_{jkl}$ is the Levi-Cavita symbol.

From the motion equations given in Equations (1) and (2), (Gertler and Hagen, 1967) developed a maneuvering model for UVs, which was later revised by (Feldman, 1979). In those models, added mass was represented by terms such as $\dot{u}X_{\dot{u}}$.

Added mass/inertia of finned axisymmetric bodies has been thoroughly investigated over the last few decades, primarily due to the geometric similarities between these bodies and modern underwater vehicles, airplanes, and missiles.

Since the theoretical derivation of added mass matrix (Equation (3)) of an immersed finned axisymmetric body by (Imlay, 1961), various methods have been developed and implemented by researchers, utilizing different theoretical backgrounds, to fill the non-zero elements of this matrix. These methods can be categorized into three main topics: Analytical-Semi Empirical (ASE) methods, Boundary Element Methods (BEM) and Computational Fluid Dynamics (CFD) methods. On the other hand, results obtained from advanced methods can also be utilized to derive empirical relations (Mai et al., 2023). A comprehensive review of the literature regarding these methods and significant contributors in each category is summarized by (Javanmard et al., 2020).

CFD methods dedicated to the determination of added mass matrix of an underwater body consist of two subcategories. Although more sophisticated studies have been performed recently using "synthetic" motions of underwater bodies (Foroushani & Sabzpooshani, 2021), oscillatory motion methods aim to mimic the motion produced by experimental facilities such as the Conning Motion Mechanism (CMM) or the Planar Motion Mechanism (PMM). The analyses are performed in the frequency domain rather than in time and required the post-procession of the results. Since these type of analyses involve mesh motion or deformation, they are computationally expensive and difficult to set up. Major contribution to this subcategory have been made by (Phillips et al., 2007; Sakamoto, 2009; Tang et al., 2009; Zhang et al., 2010; Kim et al., 2015; Moelyadi et al., 2018; Kahramanoglu, 2023).

Another subcategory involves analyses performed in the time domain and does not involve mesh motion or deformation. In these types of analyses, the underwater body is exposed to a variable forward speed over time. In a CFD environment, this can be achieved by defining a time-dependent velocity inlet boundary condition while the vehicle is at rest. The major contributions to this subcategory has been made by (Cimbala, 2003; Mishra et al., 2011; Javanmard et al., 2020).

A time-dependent velocity inlet boundary condition consists of steady and acceleration phases, as used in previous studies (Cimbala, 2003; Mishra et al., 2011), on axisymmetric geometries in order to calculate $m_{11}$. However, using a velocity inlet boundary condition that only consists of steady and acceleration phases can introduce history effects and may lead to bias/errors in the results(Javanmard et al., 2020).

In order to eliminate history effects, (Javanmard et al., 2020) used a velocity inlet boundary condition that also includes a deceleration phase. By doing this, peaks in the force vs. time curve at the transitions to steady motion and accelerated/decelerated motion cancel each out. Since peaks are the main source of history effects, this approach successfully eliminates this error from the results.

In this study, the surge added mass ($m_{11}$) of a fully appended generic submarine geometry (DARPA Suboff AFF-8) is calculated using Unsteady Reynolds Averaged Navier Stokes (URANS) simulations performed with the Open-Source CFD Software OpenFOAM (Weller et. Al., 1998). The methodology proposed by (Javanmard et al., 2020) is adopted, and the velocity boundary condition at the inlet of the control volume determined accordingly. A second analysis with a different velocity inlet boundary condition is performed to demonstrate the independence of the result from the magnitude of the acceleration vector. The obtained results are then compared with the existing literature.

In the second part of the study, the surge added mass of the aforementioned geometry is calculated using the potential flow solver potentialFoam, which is embedded in OpenFOAM. potentialFoam is a solver that solves for the velocity potential to calculate the volumetric face-flux field, from which the velocity field is obtained by reconstructing the flux (OpenFOAM, 2022). This solver is commonly used in conjunction with a RANS solver to obtain an initial condition for the velocity and pressure fields. The results of the potential flow analysis are then compared with the CFD results.

After the competition of calculation of $m_{11}$, added mass coefficients in other degrees of freedom are calculated in the third part. (Javanmard et al., 2020) calculated $m_{22}$ of an UV by applying their surge added mass method on a new grid, which takes into account the change in the orientation of the vehicle with respect to incoming flow. To avoid the cumbersome task of generating a mesh for each degree of freedom, an overset version of the potentialFoam solver called overPotentialFoam is implemented.

For this type of analysis, UV (DARPA Suboff AFF-8) is placed in a spherical domain ($D_{Sphere}$= 2.35L) located on top of a cuboid background domain (4L x 3L x 3L). The overset part of the mesh is pre-rotated according to the degree of freedom for which the analysis is performed. The control volume set up for $m_{22}$ and $m_{33}$ is demonstrated in Figure 6 and Figure 7 in Section 3.2. respectively.

## 2. METHODOLOGY

The method proposed by (Javanmard et al., 2020) was applied to perform CFD analysis in time domain using the unsteady RANS solver pisoFoam. A structural computational mesh is created using snappyHexMesh, and its quality is validated through drag calculation results of the geometry under consideration.

$$F_j = -\dot{U}_i m_{ij} - \varepsilon_{jkl} U_i \Omega_k m_{li} \tag{1}$$

$$M_j = -\dot{U}_i m_{j+3,i} - \varepsilon_{jkl} U_i \Omega_k m_{l+3,i} - \varepsilon_{jkl} U_k U_i m_{li} \tag{2}$$

The surge added mass is calculated and validated against the previously published results of (Lin and Liao, 2011). The sensitivity of the results to the velocity inlet boundary condition, (i.e. magnitude of the acceleration vector) is investigated using a second acceleration profile.

$$m_{added\,[6x6]} = \begin{bmatrix} X_{\dot{u}} & 0 & 0 & 0 & 0 & 0 \\ 0 & Y_{\dot{v}} & 0 & Y_{\dot{p}} & 0 & Y_{\dot{r}} \\ 0 & 0 & Z_{\dot{w}} & 0 & Z_{\dot{q}} & 0 \\ 0 & K_{\dot{v}} & 0 & K_{\dot{p}} & 0 & K_{\dot{r}} \\ 0 & 0 & 0 & 0 & M_{\dot{q}} & 0 \\ 0 & N_{\dot{v}} & 0 & N_{\dot{P}} & 0 & N_{\dot{r}} \end{bmatrix} \tag{3}$$

Methods based on the potential theory are known to have good performance in predicting added mass coefficients. However, predicting the velocity potential of complex geometries can be tedious or even impossible. To overcome this difficulty, the potential flow solver potentialFoam, available in OpenFOAM, is utilized. The resulting velocity field around the submarine is then used to calculate the difference in the kinetic energy of the medium inside the control volume. This energy difference is closely related with to the definition of the added mass. Following the procedure defined in (Konstantinidis, 2013), the change in kinetic energy of the fluid due to the motion of the body can be defined as shown in Equation (4);

$$E_K = \frac{1}{2}\rho \oint_V (u - U_\infty)_i (u - U_\infty)_i dV \tag{4}$$

The CFD results obtained in the first step of the study using pisoFoam are then utilized to validate the results of potentialFoam.

Due to the change in orientation of the vehicle, a new computational mesh is required for each degree of freedom in above-proposed CFD procedure. However, an alternative approach is adopted by utilizing an overset mesh configuration in conjunction with the overPotentialFoam solver. The added mass coefficients in the sway ($m_{22}$) and heave ($m_{33}$) degrees of freedom are calculated using this modified setup and validated against existing literature.

## 3. CFD SIMULATIONS

### 3.1 GOVERNING EQUATIONS

The analysis in the time domain, utilizing a time-dependent velocity inlet boundary condition, is governed by the incompressible form of the unsteady RANS equations, i.e. the continuity equation (Equation (5)) and the momentum equation (Equation (6)).

$$\frac{\partial \bar{U}_i}{\partial x_i} = 0 \tag{5}$$

$$\frac{\partial \bar{U}_i}{\partial t} + \frac{\partial \overline{U_\iota U_J}}{\partial x_j} = -\frac{1}{\rho}\frac{\partial P}{\partial x_i} + \frac{\partial}{\partial x_j}\left\{\nu\left(\frac{\partial \bar{U}_i}{\partial x_j} + \frac{\partial \bar{U}_j}{\partial x_i}\right)\right\} - \frac{\partial \overline{U_\iota' U_J'}}{\partial x_j} + f_i \tag{6}$$

Where $\bar{U}_\iota$ is the velocity of the flow, P is the pressure, $\nu$ is the effective viscosity (i.e. the superposition of molecular and artificial viscosity arising from turbulence), $\rho$ represents the fluid density (which is constant by definition) and $f_i$ represents the external force effects in the "i" direction.

In order to close the system of governing equations, the Reynolds Stress Term (i.e. $\overline{U_\iota' U_J'}$) is modeled using the k-ε turbulence model. The k- ε turbulence model is a high Reynolds Number turbulence model. It does not require a special near-wall treatment, resulting in a reasonably low mesh count and computational cost. When dealing with integral quantities such as forces, this represents a reasonable compromise.

For incompressible steady-state potential flows solved using potentialFoam and overPotentialFoam, the governing equation for the velocity potential satisfies the Laplace's Equation (7).

$$\nabla^2 \Phi = 0 \tag{7}$$

where Φ is the velocity potential. The velocity field (i.e. u) can then be computed from the velocity potential as shown in Equation (8).

$$u = \nabla\Phi \tag{8}$$

where the velocity field is solenoidal (Equation (9)):

$$\nabla \cdot u \tag{9}$$

### 3.2 GEOMETRY

Simulations are performed on the fully-appended DARPA Suboff Geometry (Figure 1). The geometric characteristics of the vehicle were defined by (Groves et al., 1989) and are provided in Table 1. Here L is the overall length of the UV $D_{max}$ is the maximum dimeter of the hull, H is the sail height from the symmetry axis $\nabla$ is the displacement and $\lambda$ is the scale factor.

**Table 1:** Basic Characteristics of DARPA Suboff.

| | |
|---|---|
| L | 4.356 m |
| $D_{max}$ | 0.508 m. |
| H | 0.460 m |
| $\nabla$ | 0.718 $m^3$ |
| $\lambda$ | 1/24 |

**Figure 1:** DARPA Suboff AFF-8.

### 3.3 DOMAIN, MESH GENERATION AND BOUNDARY CONDITIONS

A structural mesh is generated using the native hexagonal mesh tool of OpenFOAM, known as snappyHexMesh, around the UV geometry. A rectangular prism with dimensions of 5L x 10D x 10D is choosen as the control volume to confine the fluid domain, which is essentially infinite by definition. Here, L represents the characteristic length and D represents the maximum diameter of the UV. The meshing process consists of three steps: first, a castellated mesh is formed, then cells are deformed to snap the geometry precisely and finally an inflation layer is added. This results in a mesh with a total cell count of 4.6 million, which is used for both drag and added mass calculations. For the potential flow calculations the las phase of the meshing process is omitted. Resulting mesh has a 0.7 million cell count. The boundary conditions remain the same, except at the inlet boundary condition used in unsteady computations.

Monotonic convergence is achieved for the steady calculations (Drag) whereas unsteady data has oscillations. Computational cost regarding an unsteady calculation (i.e. for a single acceleration profile) is around 4700 CPU x hour at the at UHeM (National Center of High Performance Computing) cluster. For steady calculations this cost reduces to 700 CPU x hour. The computational cost for the potential flow calculations is not significant. Required time for the calculations are on the order of minutes.

The domain extends one boat length in front of the UV and three boat lengths in the leeward direction. The front boundary serves as the velocity inlet, where the velocity vector points in the positive "x" direction, and its magnitude varies with respect to time. The pressure outlet boundary is located in the leeward direction, where the flow exists the control volume. The side and top/bottom boundaries are positioned at an equal distance form the UV centerline, and symmetry boundary conditions are assigned to them to assume parallel flow.

The velocity field is enforced to satisfy the no-slip and no-penetration boundary conditions on the UV surface. The low turbulence zone in close proximity of the UV, which the selected turbulence model (i.e. k-ε model) cannot perform well, is bridged with a wall-function approximation. First cell height of the computational mesh is chosen based on this approximation, with a dimensionless value raging between 30 and 300 across the UV surface. The distribution of the nondimensional wall distance on the UV surface is illustrated in Figure 2. The generated mesh and near-wall field can be observed in Figure 3 and Figure 4. The boundary conditions are presented in Figure 3.

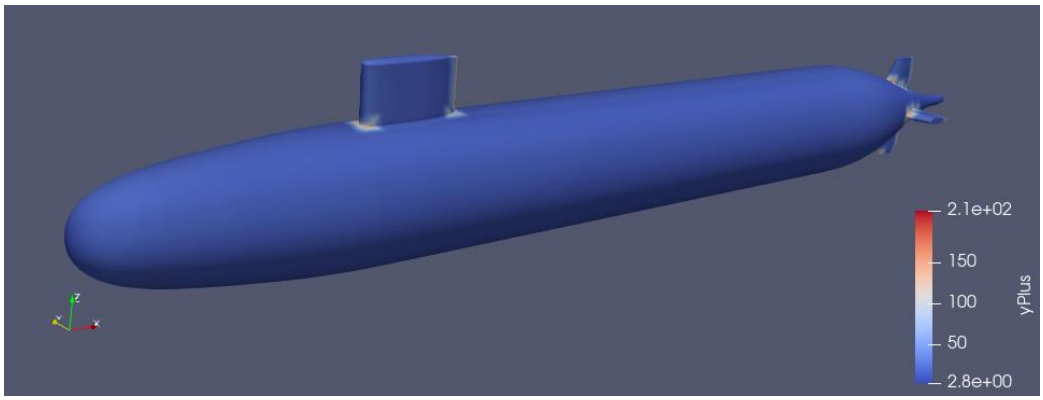


**Figure 2:** Nondimensional Wall Distance Distribution on UV Surface.

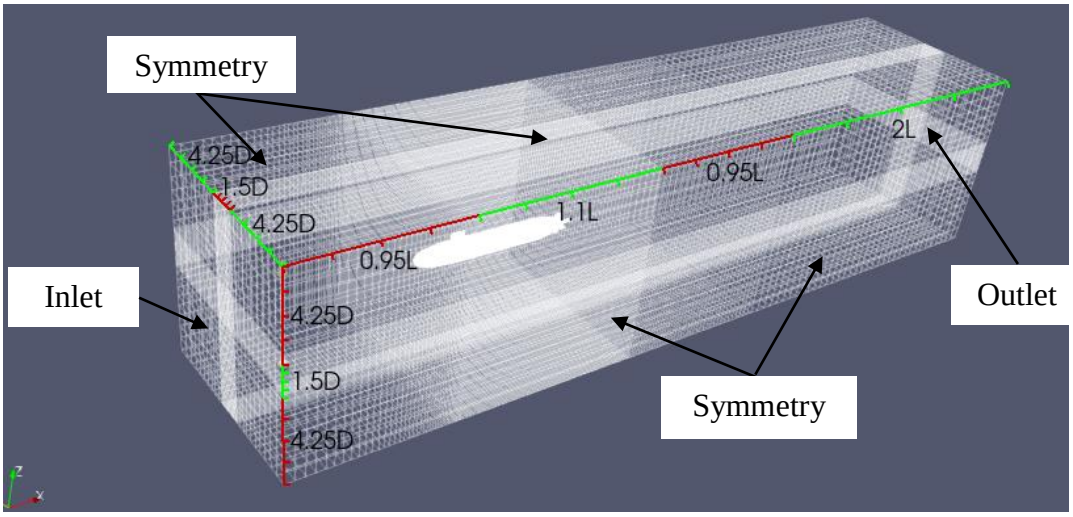


**Figure 3:** Control Volume and Computational Mesh.

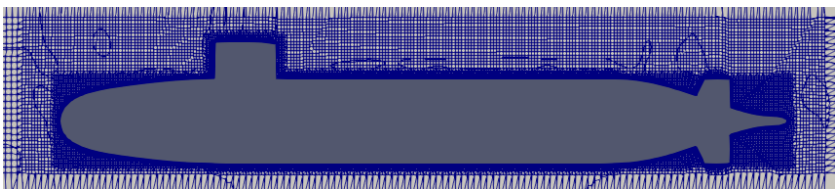

**Figure 4:** Near-wall Mesh.

For the cases where overPotentialFoam is utilized (i.e. for the calculation of $m_{22}$ and $m_{33}$) the general layout of the control volume, overset and background mesh zones and the orientation of the UV are illustrated in Figure 5 to Figure 7.

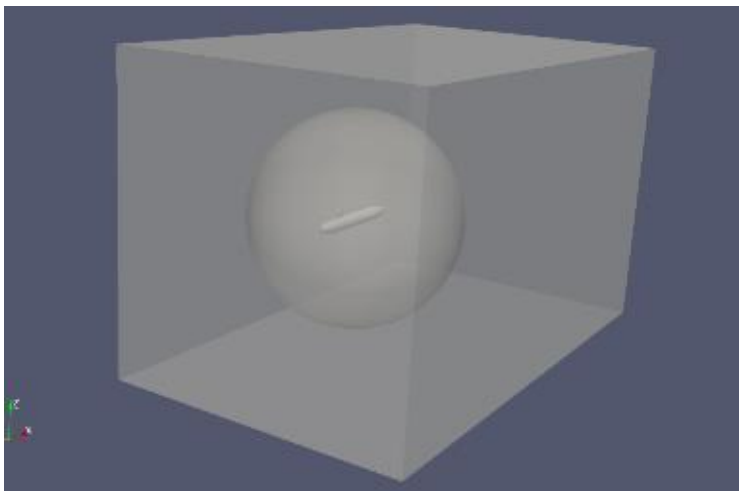

**Figure 5:** General Layout of the Control Volume for Inviscid Calculations.

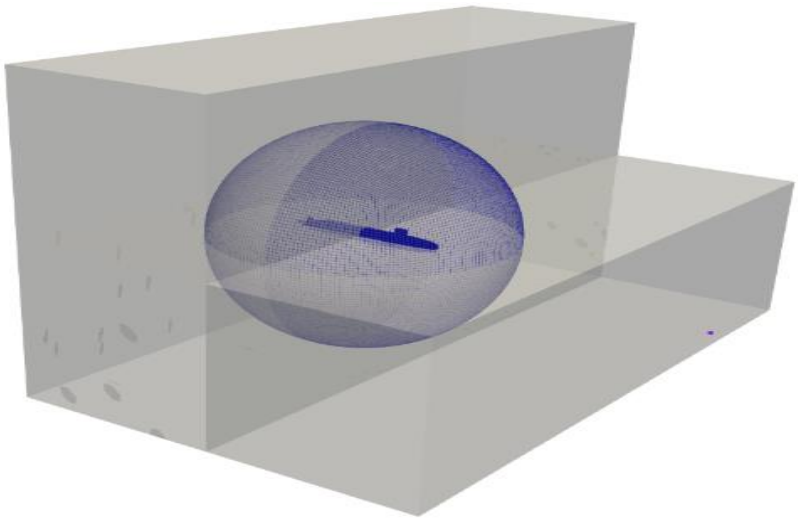

**Figure 6:** Orientation for Calculation $m_{22}$.

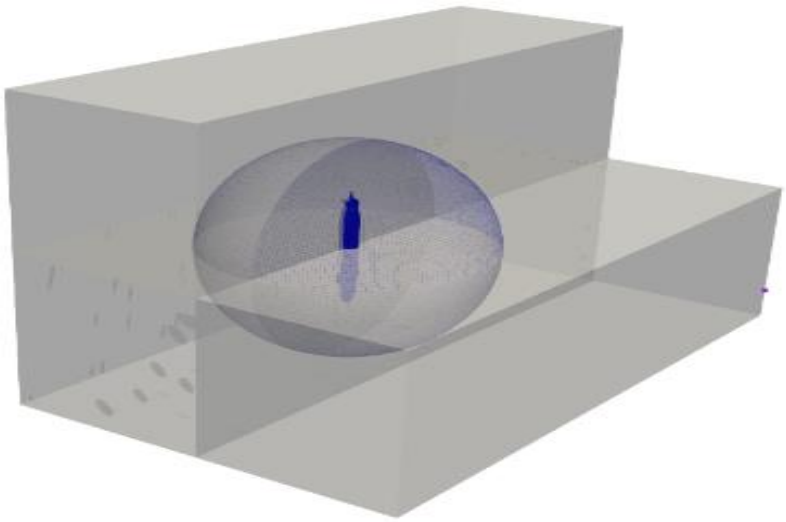

**Figure 7:** Orientation for Calculation $m_{33}$.

### 3.4 MESH VALIDATION AND INDEPENDENCY

The computational performance and ability to produce accurate results of the mesh are validated through the comparison of highly accepted quantities in the literature, such as drag, pressure and skin friction coefficients. Drag calculations are made for the speed range of 2-10 m/s and based on superposition of viscous and pressure drag. While the former one is due to the skin friction and the latter one is basically the integration of pressure distribution on the UV surface. The obtained results are then compared with the experimental results of (Crook, 1990) and (Liu and Huang, 1998), as depicted in Figure 8.

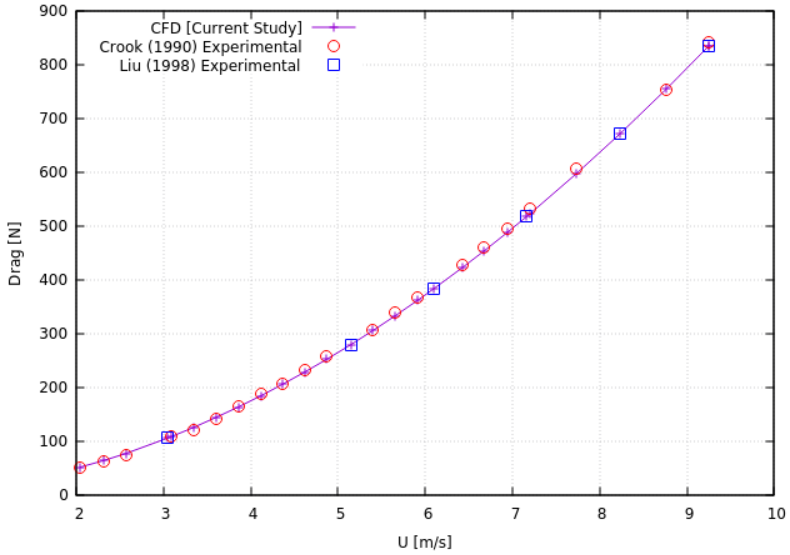


**Figure 8:** Comparison of the CFD results with Crook (1990) and Liu and Huang (1998).

Pressure and skin friction coefficient distributions are obtained for the upper meridian line of the UV and compared with the results of (Huang and Liu, 1994; Qiu et al., 2018) respectively. The results are dispayed in Figure 9 and Figure 10. The level of agreement between the results is satisfactory. The asymptotic behaviour of the numerical data at the leading edge of the UV's sail (at x/L = 0.2) is due to the formation of a stagnation point at this location. Flow velocity is zero and the pressure equals to stagnation pressure (which can get very high values) at this point. Sensor locations in the experimental setup is chosen right before and after this point (Groves et al., 1989) considering above mentioned phenomena and thus can not demonstrate the same behavior captured in the numerical analysis.

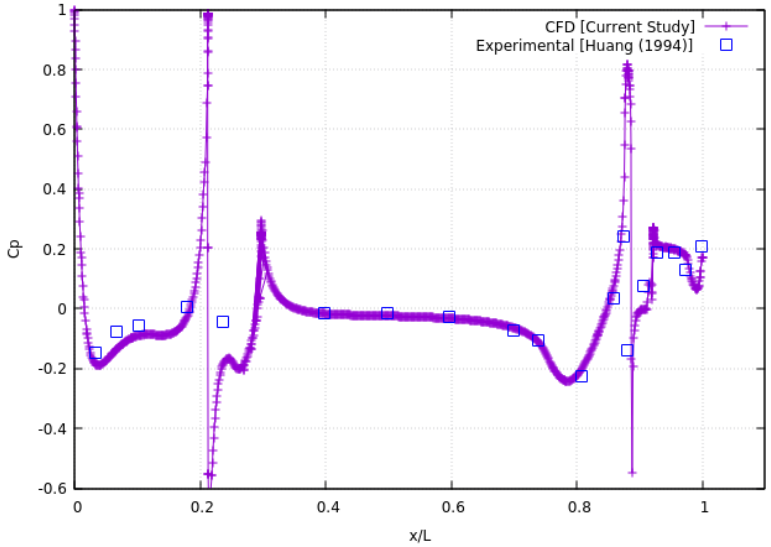


**Figure 9:** Pressure Coefficient Distribution on the Upper Meridian Line of UV.

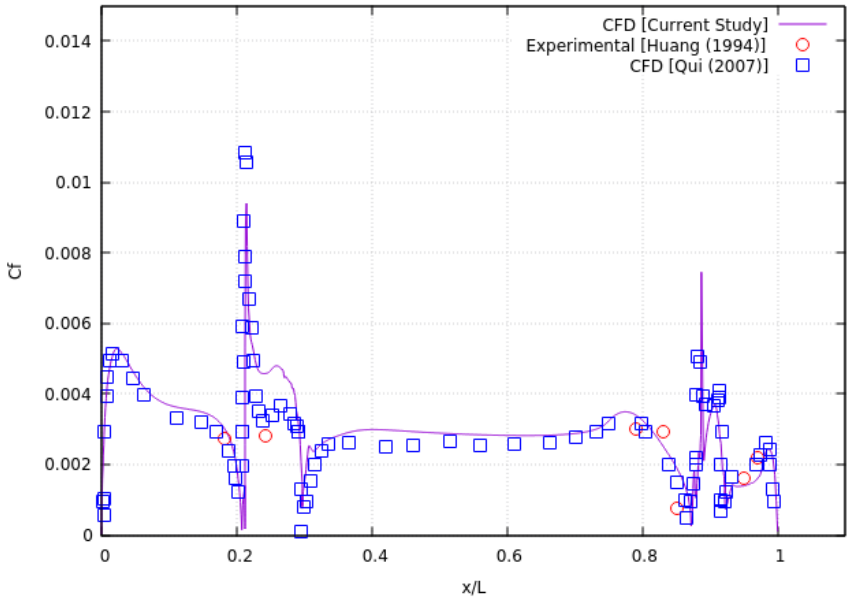


**Figure 10:** Skin Friction Coefficient Distribution on the Upper Meridian Line of the UV.

## 4. RESULTS

### 4.1 VISCOUS FLOW CALCULATIONS

Unsteady RANS (URANS) analyses are conducted on the fully appended DARPA Suboff geometry to determine the surge added mass. The method developed by (Javanmard et al., 2020) is adapted and the transient solver (pisoFoam) of the open-source CFD code OpenFOAM is employed. The method involves subjecting the geometry to a time dependent velocity profile (as shown in Figure 11 and Figure 13), which consists of accelerating, steady and decelerating phases, and measuring the resulting variation in drag force.

As can be observed from the Figure 11 and Figure 13, during the decelerating phase of the velocity profile, there is a point in the time where the vehicle reaches the initial velocity of $U_0$. At this moment, the hydrodynamic force acting on the vehicle consists of both the drag force of the vehicle at U(t) = $U_0$ and the inertia force of the fluid surrounding the decelerating vehicle, resulting from the added mass effect. Therefore, the difference between the hydrodynamic force at time "t" where U(t) = $U_0$ in decelerating phase and drag force of the vehicle represents the fluid inertia force, as demonstrated in Equation (10) and (11).

$$\left|F_{V=V_0} - F_{Drag}\right| = (\rho\nabla + m_a)|a| \tag{10}$$

$$m_a = \frac{\left|F_{V=V_0} - F_{Drag}\right|}{a} - \rho\nabla \tag{11}$$

The aforementioned velocity profile is applied as an inlet boundary condition. All transient calculations are initialized with the previously calculated steady-state result of the same speed in order to accelerate convergence. The deviation in the drag force is attributed to the accelerated flow field. This difference in the drag force is then used to calculate the added mass of the body.

The first velocity profile applied as an inlet boundary condition (Figure 11) is based on an acceleration value of 0.5 m/s$^2$.

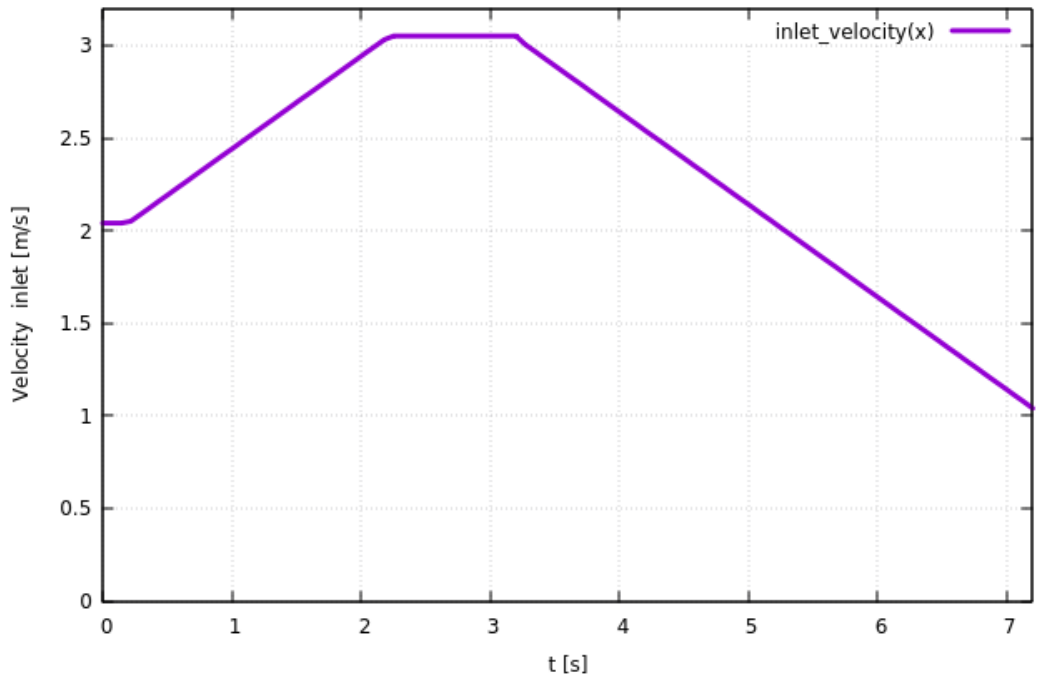


**Figure 11:** 1st Velocity Profile at Inlet.

The corresponding piece-wise function is given in Equation (12). The $U_0$ values are selected from those that have benchmark drag results. Experimental drag results for these velocity values are also marked on Figure 12 and Figure 14.

$$U(t) = \begin{cases} 2.0405 \; 0 < t < 0.2 \\ 0.5t + 1.9405 \; 0.2 < t < 2.2 \\ 3.0504 \; 2.2 < t < 3.2 \\ -0.5(t - 3.2) + 3.0504 \; 3.2 < t < 7.2 \end{cases} \tag{12}$$

The URANS analyses are performed using the k-ε turbulence model. Consequently, the inlet boundary conditions for turbulent kinetic energy (k) and dissipation rate (ε) must also be functions of time. Assuming turbulence intensity (I) of %1.5 $C_\mu$=0.09 and β=5, k and ε are calculated using Equations (13) and (14).

$$k = 1.5(IU)^2 \tag{13}$$

$$\varepsilon = \frac{C_\mu k^2}{\beta \nu} \tag{14}$$

Applying these inlet boundary conditions, the resulting drag force vs. time graph is shown in Figure 12. At the beginning of the acceleration phase (at t=0.2 s), when U=2.0405 m/s, the drag force is calculated as 50.6557 N. Following the acceleration, steady and deceleration phases (at t=5.2005 s), the drag force is measured as -316.747 N for the same speed.

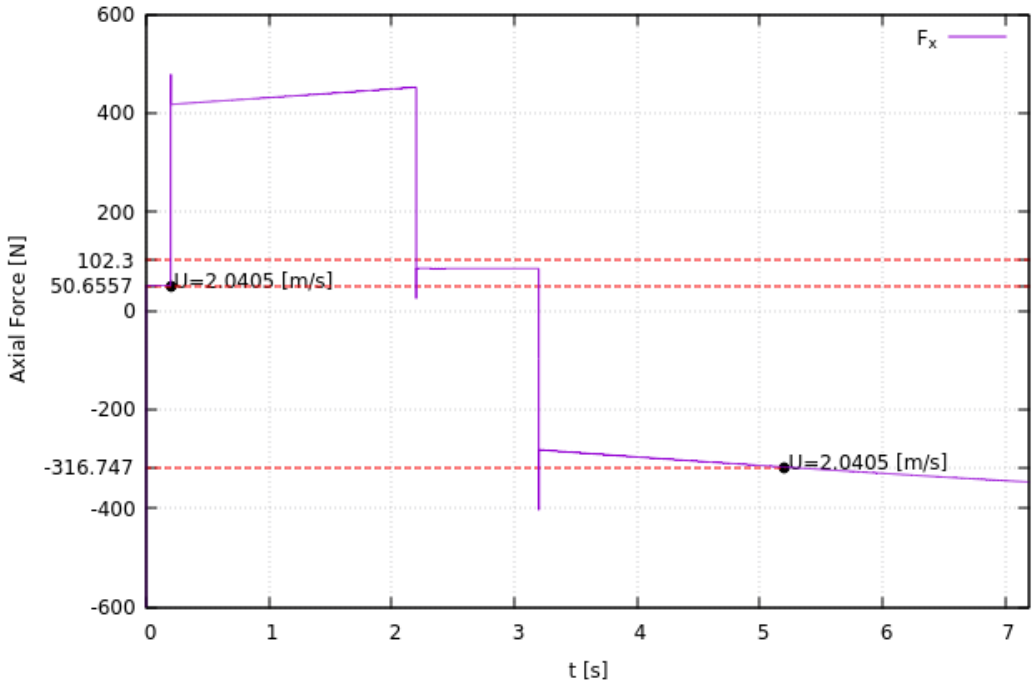


**Figure 12:** Axial Force Variation with Time.

By utilizing these two values, the added mass of the fully appended DARPA Suboff submarine is calculated according to Equation (15).

$$\frac{|F_{t=5.2005} - F_{t=0.2}|}{|\dot{u}|} - \rho\nabla = 30.8903kg \tag{15}$$

To validate the performed analysis and demonstrate the independence of the results from the inlet velocity profile (magnitude of the acceleration vector), another analysis is carried out using a different velocity profile (a=0.75 m/s$^2$). The second velocity profile and its corresponding piece-wise function are provided in Figure 13 and Equation (16), respectively.

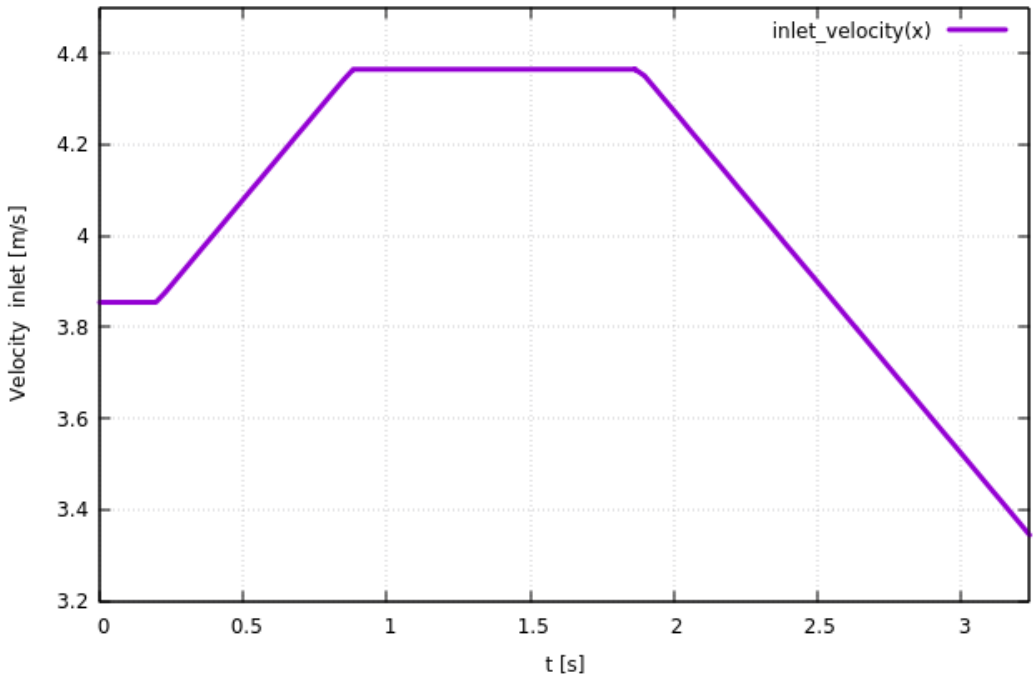


**Figure 13:** 2nd Velocity Profile at Inlet.

Resulting drag force vs. time graph can be observed in Figure 14.

$$U(t) = \begin{Bmatrix} 3.8540 < t < 0.2 \\ 0.75t + 3.7040.2 < t < 0.88 \\ 4.364\ 0.88 < t < 1.88 \\ -0.75(t - 1.88) + 4.364\ 1.88 < t < 3.24 \end{Bmatrix} \quad (16)$$

In Figure 14, at the beginning of the acceleration phase (at t=0.2 s) where U=3.854 m/s, the drag force is calculated as 162.66 N. Following the acceleration, steady and deceleration phases (at t=2.56 s), the drag force is measured as -388.353 N for the same speed. Utilizing these two values, the added mass of the fully appended DARPA Suboff submarine is calculated according to Equation (17).

$$\frac{|F_{t=2.56} - F_{t=0.2}|}{|\dot{u}|} - \rho\nabla = 30.7695kg \quad (17)$$

The difference between these two values is approximately % 0.4. This demonstrates that the performed analyses are independent of the chosen acceleration value.

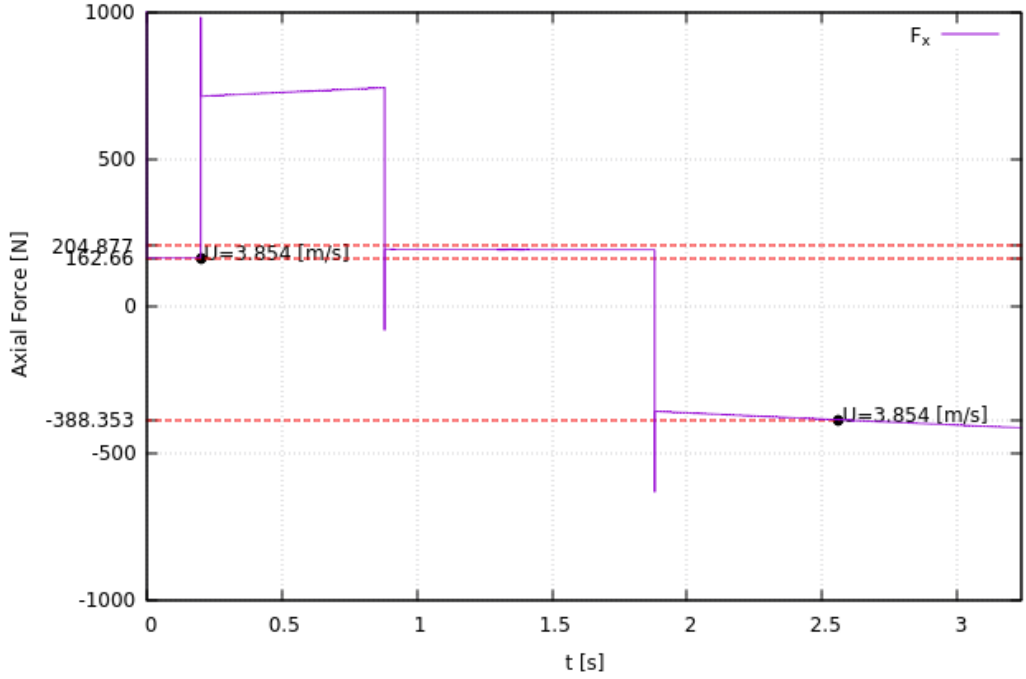


**Figure 14:** Axial Force Variation with Time.

## 4.2 INVISCID FLOW CALCULATIONS

Since potential theory is known for its good performance in predicting added mass, the potential flow solver of the OpenFOAM, namely potentialFoam, is utilized. Following the procedure defined in (Konstantinidis, 2013), the change in kinetic energy of the fluid due to the motion of the body is calculated using Equation (18).

$$m_{11} = \frac{2E_k}{U_\infty^2} = 29.4068kg. \quad (18)$$

Comparison of this value with the results of transient calculations and the results obtained by (Lin and Liao, 2011), gives a difference of % 4.8 and % 9.99 respectively. These differences are within an acceptable range for an engineering solution.

For the sway and heave degrees of freedom, the added mass values are computed using overPotentialFoam to avoid the need of remeshing the control volume due to the changes in the vehicle's orientation. The calculation process is straightforward, but it is important to ensure that the kinetic energy change in the overset zone is not calculated twice to ensure accurate simulations. The results are presented in Table 2, with a difference of approximately 2%, which is highly acceptable.

**Table 2:** Comparison of the Results.

| Added Mass (Inviscid) [kg.] | (Lin & Liao, 2011) [kg.] | Error [%] |
|---|---|---|
| $m_{11}$ = 29.407 | 26,736 | 9.99 |
| $m_{22}$ = 714.86 | 701.62 | 1.89 |
| $m_{33}$ = 673.23 | 661.65 | 1.75 |

## 5. CONCLUSIONS

This study aims to demonstrate the effectiveness of open source CFD software OpenFOAM solvers for calculating the added mass coefficients of a generic submarine geometry. The method proposed by (Javanmard et al., 2020) is applied to perform CFD analyses in the time domain using the unsteady RANS solver pisoFoam. A structural computational mesh is created using snappyHexMesh, and its quality is validated against drag, skin friction coefficient and pressure coefficient distribution calculation results in the Literature. The Surge added mass is calculated and validated against the results of (Lin and Liao, 2011). The sensitivity of the results to the velocity inlet boundary condition is investigated by using a second acceleration profile. The results indicate that there is no correlation between the magnitude of the acceleration vector and the value of the added mass.

The potential flow solver of OpenFOAM, namely potantialFoam, is utilized. The resulting velocity field around the submarine is then used to calculate the difference in the kinetic energy of the fluid inside the control volume, as the definition of the added mass is closely related with this energy difference. The CFD results obtained in the first step of the study using pisoFoam are then used to validate the results obtained from potentialFoam. The level of agreement between the results from the two different solver and the results from (Lin and Liao, 2011) is found to be satisfactory.

Since a new computational mesh is required in each degree of freedom due to the change in orientation of the vehicle, an overset mesh configuration is adopted along with the overPotentialFoam solver to avoid this cumbersome task. The added mass coefficients in the sway ($m_{22}$) and heave ($m_{33}$) degrees of freedom are calculated using this modification and validated against the literature. The level of accuracy achieved is acceptable from an engineering point of view. Potential flow solutions offer computational efficiency compared to URANS simulations and provide superior accuracy compared to ASE methods. Additionally, the straightforwardness of the pre-processing phase, when compared to BEM methods, gives potential flow methods an added advantage. With this perspective, the proposed method can be used as an alternative to both types of URANS simulations and experimental methods due to its computational efficiency, low cost, and high level of accuracy.

Authors intended to investigate the applicability of the proposed method in the existence of a free surface boundary condition in the near future.

## 6. REFERENCES

Cimbala, J.M., (2003). A new method for calculating added mass using CFD. In: Proceedings, Division of Fluid Dynamics 56th Annual Meeting. East Rutherford, New Jersey.

Crook, B. (1990). Resistance for DARPA SUBOFF as Represented by Model 5470. David Taylor Research Center, Bethesda, Md.

Feldman, J. (1979). DTNSRDC Revised Standard Submarine Equations of Motions. (DTNSRDC SPD-0303-09). David W. Taylor Naval Slu'p Research and Development Center.

Foroushani, J. A., & Sabzpooshani, M. (2021). Determination of hydrodynamic derivatives of an ocean vehicle using cfd analyses of synthetic standard dynamic tests. Applied Ocean Research, 108(January), 102539. https://doi.org/10.1016/j.apor.2021.102539

Gertler, M., and Hagen, G. R. (1967). Standart Equations of Motion For Submarine Simulation. (No. Report 2510). Naval Ship Research and Development Center.

Groves, N. C., Huang, T. T., & Chang, M. S. (1989). Geometric Characteristics of DARPA (Defense Advanced Research Projects Agency) SUBOFF models (DTRC model numbers 5470 and 5471). David Taylor Research Center Bethesda MD Ship Hydromechanics Dept.

Huang, T., and Liu, H. L., (1994) Measurements of flows over an axisymmetric body with various appendages in a wind tunnel: the DARPA SUBOFF experimental program.

Imlay, F. H. (1961). The Complete Expressions for Added Mass of a Rigid Body Moving in an Ideal Fluid (No. Report 1528). United States Department of the Navy, David Taylor Model Basin.

Javanmard, E., Mansoorzadeh, S., & Mehr, J. A. (2020). A new CFD method for determination of translational added mass coefficients of an underwater vehicle. Ocean Engineering, 215(August), 107857. https://doi.org/10.1016/j.oceaneng.2020.107857

Konstantinidis, E. (2013). Added mass of a circular cylinder oscillating in a free stream Subject Areas : In Proceedings of the Royal Society A: Mathematical, Physical and Engineering Sciences, 469(2156), 20130135.

Lin, Z., and Liao, S. (2011). Calculation of Added Mass Coefficients of 3D Complicated Underwater Bodies by FMBEM. Communications in Nonlinear Science and Numerical Simulation, 16(1), 187–194. https://doi.org/10.1016/j.cnsns.2010.02.015

Liu, H., and Huang, T. T. (1998). Summary of DARPA Suboff Experimental Program Data. Retrieved from http://books.google.de/books?id=0Pu-SgAACAAJ&dq=intitle:Summary of DARPA Suboff Experimental Program Data&cd=1&source=gbs_api

Mai, T.L., Jeon, M., Vo, A.K., Yoon, H.K., Kim, S., Lee, J., (2023). Establishment of empirical formulae for hydrodynamic derivatives of submarine considering design parameters. International Journal of Naval Architecture and Ocean Engineering. https://doi.org/10.1016/j.ijnaoe.2023.100537

Mishra, V., Vengadesan, S., Bhattacharyya, S.K., (2011). Translational added mass of axisymmetric underwater vehicles with forward speed using computational fluid dynamics. J. Ship Res. 55, 185–195.

Moelyadi, M. A., & Riswandi, B. B. (2018). CFD based added mass prediction in cruise condition of underwater vehicle dynamic. In Journal of Physics: Conference Series (Vol. 1005, No. 1, p. 012011). IOP Publishing.

OpenFOAM, 2022. User Guide. Version v2212. OpenCFD Limited., USA.

Phillips, A., Furlong, M., Turnock, S.R., (2007). The use of computational fluid dynamics to determine the dynamic stability of an autonomous underwater vehicle. In: 10th Numerical Towing

Tank Symposium (NuTTS'07), pp. 6–11. Hamburg, Germany.

Qiu, L. Y., Shi, Z. K., Hou, G. X., & Wei, F. F. (2007). Validation of numerical simulation of the flow over submarine geometries with full appendages. Chuanbo Lixue (Journal of Ship Mechanics), 11(3), 341-350.

Sakamoto, N., (2009). URANS, DES Simulations of Static and Dynamic Manoeuvring for Surface Combatant. Ph.D. thesis. University of Iowa.

Tang, S., Ura, T., Nakatani, T., Thornton, B., Jiang, T., (2009). Estimation of the hydrodynamic coefficients of the complex-shaped autonomous underwater vehicle TUNA-SAND. J. Mar. Sci. Technol. 14, 373–386. https://doi.org/10.1007/s00773-009-0055-4.

Techet, A.H. (2005). Hydrodynamics Lecture Notes, MIT. Retrieved from https://ocw.mit.edu/courses/mechanical-engineering/2-016-hydrodynamics-13-012-fall-2005/download-course-materials/

Weller, H. G., Tabor, G., Jasak, H., & Fureby, C. (1998). A tensorial approach to computational continuum mechanics using object-oriented techniques. Computers in physics, 12(6), 620-631.

Zhang, H., Xu, Y.R., Cai, H.P., (2010). Using CFD software to calculate hydrodynamic coefficients. J. Mar. Sci. Appl. 9, 149–155. https://doi.org/10.1007/s11804-010-9009-9.